Observations of the *Hubble Deep Field* with the *Infrared Space Observatory* - I. Data reduction, maps and sky coverage

Mon. Not. R. Astron. Soc. **289,** 457–464 (1997)

Observations of the *Hubble Deep Field* with the *Infrared Space Observatory* – I. Data reduction, maps and sky coverage

S. B. G. Serjeant,[1] N. Eaton,[1] S. J. Oliver,[1] A. Efstathiou,[1] P. Goldschmidt,[1] R. G. Mann,[1] B. Mobasher,[1] M. Rowan-Robinson,[1] T. J. Sumner,[1] L. Danese,[2] D. Elbaz,[3] A. Franceschini,[4] E. Egami,[5] M. Kontizas,[6] A. Lawrence,[7] R. McMahon,[8] H. U. Norgaard-Nielsen,[9] I. Perez-Fournon[10] and J. I. Gonzalez-Serrano[11]

[1]*Astrophysics Group, Imperial College London, Blackett Laboratory, Prince Consort Road, London SW7 2BZ*
[2]*SISSA, Via Beirut 2-4, Trieste, Italy*
[3]*Service d'Astrophysique, Saclay, 91191, Gif-sur-Yvette Cedex, France*
[4]*Osservatorio Astronomico di Padova, Vicolo dell'Osservatorio 5, I-35 122, Padova, Italy*
[5]*Max-Planck-Institut für Extraterrestrische Physik, Giessenbachstrasse, D-8046, Garching bei Munchen, Germany*
[6]*Astronomical Institute, National Observatory of Athens, PO Box 200048, GR-118 10, Athens, Greece*
[7]*Institute for Astronomy, University of Edinburgh, Blackford Hill, Edinburgh EH9 3HJ*
[8]*Institute of Astronomy, The Observatories, Madingley Road, Cambridge CB3 0HA*
[9]*Danish Space Research Institute, Gl, Lundtoftevej 7, DK-2800 Lyngby, Copenhagen, Denmark*
[10]*Instituto de Astrofisica de Canarias, Via Lactea, E-38200 La Laguna, Tenerife, Canary Islands, Spain*
[11]*Instituto de Fisica de Cantabria, Santander, Spain*

Accepted 1997 May 9. Received 1997 March 24; in original form 1996 December 5

ABSTRACT

We present deep imaging at 6.7 and 15 μm from the CAM instrument on the *Infrared Space Observatory* (*ISO*), centred on the *Hubble Deep Field* (HDF). These are the deepest integrations published to date at these wavelengths in any region of sky. We discuss the observational strategy and the data reduction. The observed source density appears to approach the CAM confusion limit at 15 μm, and fluctuations in the 6.7-μm sky background may be identifiable with similar spatial fluctuations in the HDF galaxy counts. *ISO* appears to be detecting comparable field galaxy populations to the HDF, and our data yield strong evidence that future infrared missions (such as *SIRTF*, *FIRST* and *WIRE*) as well as SCUBA and millimetre arrays will easily detect field galaxies out to comparably high redshifts.

Key words: surveys – galaxies: formation – infrared: galaxies.

1 INTRODUCTION

The *Infrared Space Observatory* (*ISO*: Kessler et al. 1996) offers an improvement of orders of magnitude in sensitivity over the *IRAS* satellite, at least at shorter wavelengths (< 20 μm). *ISO* is expected both to sample the intermediate-redshift ($z \sim 0.5$–1) star-forming galaxy population at lower, less extreme luminosities, and to detect more strongly star-forming galaxies to far higher redshifts. We used the CAM instrument on *ISO* (Cesarsky et al. 1996) in Director's discretionary time to observe the *Hubble Deep Field* (HDF: Williams et al. 1996), resulting in the deepest surveys to date at 6.7 and 15 μm. The obvious advantage of this field is the extensive multi-wavelength follow-ups either published or under way (e.g. Fomalont et al. 1996; Dickinson et al., in preparation; Cowie et al., in preparation), as well as unparallelled deep multicolour optical morphologies from the *Hubble Space Telescope* (*HST*).

The HDF galaxy population is strikingly dominated by blue objects which may be comparable to local giant H II regions, and which are consistent with significant star formation. This finding is reinforced by their largely disturbed structures. In such an interpretation, a substantial fraction of the luminosity from young massive stars is absorbed by dust and re-radiated in the mid- and far-infrared. Clearly, imaging in the mid-infrared samples the spectral energy distributions of such galaxies much closer to this significant, and perhaps dominant, contribution to the bolometric power output.

In this paper we present our CAM images of the HDF, discuss the data reduction steps and make crude comparisons of the sky fluctuations with smoothed HDF images.

Subsequent papers will address the source identification algorithm (Goldschmidt et al. 1997, hereafter Paper II); the source counts and comparison with models (Oliver et al. 1997, hereafter Paper III), including a more sophisticated treatment of the confusion noise; the associations with HDF galaxies (Mann et al. 1997, hereafter Paper IV); and the spectral energy distributions of our sources and implications for star formation history (Rowan-Robinson et al. 1997, hereafter Paper V).

The maps presented here are available at http://artemis.ph.ic.ac.uk/hdf or from the authors.

2 DATA ACQUISITION AND ANALYSIS

2.1 Observation strategy

The observing strategy was designed to reach the predicted confusion limit of CAM, using the source count models of Pearson & Rowan-Robinson (1996). The observations were performed in two bands, 6.7 and 15 μm (the LW-2 and LW-3 filters respectively), to obtain (albeit limited) colour information. These bands are the widest available in CAM, so yield the deepest possible integrations. Typically more than one HDF galaxy falls within the Airy disc, even at 6.7 μm, so sub-pixel offsets are needed to maximize the available spatial information.

We made three 8×8 rasters in microscanning mode (CAM01) analogous to the 'dithering' in the HDF, each centred on one of the HDF Wide Field (WF) frames, at both 6.7 and 15 μm, using in total ~44.9 ks of time including overheads. Our choice of 3-arcsec (6-arcsec) pixel sizes at 6.7 μm (15 μm) and raster step sizes of 5 arcsec (9 arcsec) yields optimal flat-fielding accuracy and spatial resolution. At 6.7 μm this gives a 96-arcsec field of view, well-matched to the HDF WF frames. The spacecraft jitter observed in-flight is ± 0.5 arcsec (2σ limits, half-cone), much smaller than our choices of either pixel size or step size. Cosmic ray transients (discussed below) ruled out readout integration times longer than 10 s, and the signal-to-noise ratio versus time predictions from the CAM simulator implied diminishing returns for more than 10 (20) readouts per raster position at 6.7 μm (15 μm). The number of stabilization readouts prior to the rasters at each wavelength is appropriate for 5σ sources. The Astronomical Observation Template (AOT) parameters are summarized in Table 1; for a more detailed discussion of these parameters see the SAM Observer's Manual.[1] Resulting noise levels in each of the fields are listed in Table 2. The pixel scale of ISOPHOT made longer wavelength observations impracticable.

The edited raw data FITS files (supplied by ESA) were processed using the CIA (CAM Interactive Analysis, 1996 April version) IDL package, with the exception of the deglitching, the construction of the flat-field and the mosaicking of the rasters, as discussed below.

2.2 Dark subtraction, deglitching and flat-fielding

The default dark frame in the 1996 April CIA version was subtracted from the data.

Cosmic ray events were easily identified in the readout histories of each pixel as $>4\sigma$ rises followed (one or two readouts later) by $>4\sigma$ falls. A similar algorithm was used to find readout troughs. These events were masked out in the mosaicking discussed below.

However, a minority of cosmic rays appear to cause transients in subsequent readouts with roughly exponential decays (see Fig. 1) persisting over a few readouts. These glitch transients are in general difficult to model. No attempt was made to identify and remove them; instead, they were effectively removed by median filtering in the mosaicking below.

Use of the ESA-supplied flat-field gave very unsatisfactory results. Instead, we created our own sky flat by noting that each detector pixel samples 64 different sky positions during the raster. For each detector pixel, we examined the histogram of (unmasked) readouts and fitted Gaussians to find a mean value. To eliminate both sources and glitch

[1]The CAM manual is available from http://isowww.estec.esa.nl/manuals/iso.cam/

Table 1. Summary of our CAM01 Astronomical Observation Templates (parameters defining our $M \times N$ rasters). An exposure of T_{int} is made N_{obs} times at each of the $M \times N$ raster positions. Each raster was preceded by N_{stab} readouts at the first raster position to stabilize the CAM detector.

Parameter	LW-2 6.7μm	LW-3 15μm
Pixel field of view	3″	6″
M, N steps	8, 8	8, 8
M, N step size	5″, 5″	9″, 9″
T_{int}	10 sec	5 sec
N_{stab}	80	100
N_{obs}	10	20

Table 2. Summary of calibration and sky backgrounds. Intensities quoted are in μJy per arcsec^2. The sky backgrounds in each of the fields (I_{ISO}) are compared against the model (I_{MODEL}) discussed in the text. Noise estimates assume a circular beam size of 6 arcsec for LW-2 and 12 arcsec for LW-3.

Band	λ (μm)	Width (μm)	Area	Date Observed	I_{MODEL}	I_{ISO}	1σ/ beam	Normalisation Shift/Add	Drizzle
LW-2	6.75	3.375	WF-2	28/6/1996	73.4	77.3	7.78	1.03431	1.03390
			WF-3	28/6/1996		79.9	8.59	1.01630	1.01492
			WF-4	28/6/1996		80.0	8.43	1.00000	1.00000
LW-3	14.5	4.833	WF-2	1/7/1996	508	401	36.8	1.00000	1.00308
			WF-3	1/7/1996		402	27.4	1.00255	1.00000
			WF-4	26/6/1996		396	46.1	1.01306	1.01454

transients, $>5\sigma$ outliers from the mean were eliminated and the fit was iterated.

2.3 Shift-and-add maps

The rasters were mosaicked together using two competing algorithms: drizzling (described below), and variants on shift-and-add. The latter are expected to have a higher signal-to-noise ratio but at the expense of spatial resolution.

In order to eliminate possible long-time-scale detector sensitivity drifts, the rasters were renormalized by the following method. First, we calculated the median readout in each of the 32×32 CAM pixels for each raster at each wavelength. Secondly, we found the mean in the central 11×11 of these images. This determined the relative renormalizations, which are listed in Table 2. Comparison of the source positions in each individual raster revealed a systematic offset in the WF-4 15-μm frame, probably due to a random offset in the lens positioning. For consistency with the drizzled mosaics we applied the same offset to this raster as discussed below for the drizzling.

In the shift-and-added frames, we began by defining an image with pixel size one-sixth that of the CAM detector pixels (i.e. one-sixth of 3 arcsec at 6.7 μm, and of 6 arcsec at 15 μm), encompassing the area surveyed by all three rasters. Each position in this fine-gridded image may have been observed several times by the CAM detector array, so we compiled a list of such CAM pixel readouts for each fine-gridded image position. The data at a given sky position could then (for example) be median-filtered or mean-averaged to produce a final image.

The glitch transients discussed above make a large contribution to the noise in final mosaics made by simple mean averages of readouts. An obvious alternative is median filtering, although this has a signal-to-noise ratio penalty (about $\sqrt{2}$). The glitch transients have time-scales of the order of or less than the duration of a pointing, so a possible compromise is to mean-average over pointings, and median-filter the means. This may also have the advantage of identifying affected readouts more efficiently.

Several mosaics were therefore created from the readout arrays: (i) using the median readout at each position, to eliminate glitches; (ii) using the mean readout at each position, with the $\pm 5\sigma$ outliers eliminated and iterated to eliminate glitches; (iii) using the mean readout within each raster position, followed by the median of these means; (iv) using a clipped, iterated mean of pointing means. We found the best 6.7-μm map to be the simple median-filtered image, but at 15 μm the optimal map is the median-of-means, presumably reflecting a greater sensitivity to glitch transients in the final mosaic.

2.4 Drizzled maps

The drizzled images were produced with the same code (Fruchter & Hook 1996) that was used to produce the optical *HST* images. Briefly, instead of superimposing overlapping pixels, the drizzle algorithm allows the user to shrink the input pixel sizes (the 'footprint') before superimposing. At one limit the drizzle algorithm is equivalent to interlacing; at the other it is similar to shift-and-add above. Since the *ISO* HDF images were taken with fractional pixel spacings between them, maps with increased resolution can be constructed. The footprint was chosen to produce roughly the highest resolution image without leaving gaps in the output image.

Glitch transients were first removed from the input images using the following median filtering scheme, noting that at 6.7 μm the raster step offsets correspond to $1\frac{2}{3}$ pixels and at 15 μm the offsets are $1\frac{1}{2}$ pixels. The 64 individual pointings were grouped into sets whose members have integer pixel offsets (nine groups for LW-2 and four for LW-3), and for each of these groups the medians of the data at each pixel position (allowing for the shifts) were put into

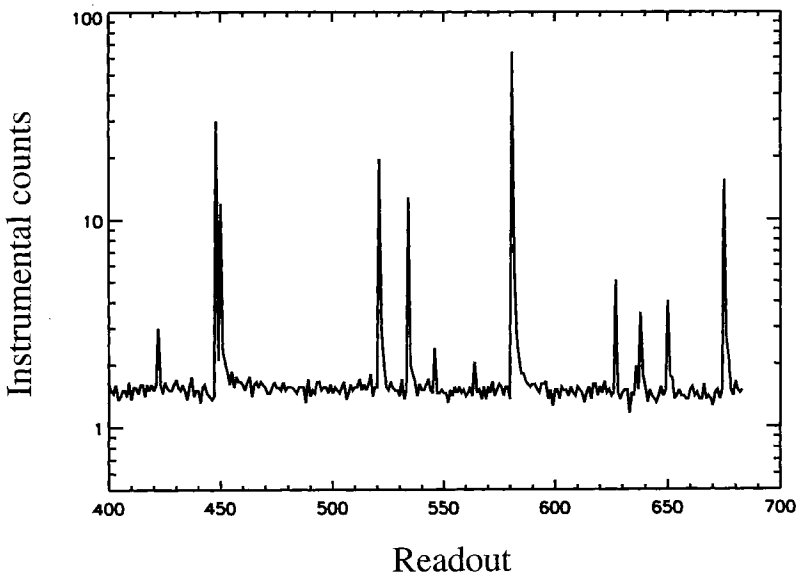

Figure 1. Examples of glitches. The data shown comprise a dark-subtracted pixel history with the (logarithmic) *y*-axis in instrumental analogue-to-digital units per second (ADU s^{-1}) and the *x*-axis in readouts. Note the clear glitches as well as the bright glitch at readout ~580 with a transient.

an image and the variance was computed. These nine images at 6.7 μm and four images at 15 μm served as input to the drizzling algorithm.

The satellite astrometry (RA, Dec. and spacecraft roll angle) from the individual pointings was combined into these (nine + four) data sets by taking the average of those pointings making up each group, after shifting them by the nominal raster offsets. This astrometry was used to define the tangent-plane projection used in the final maps.

The *ISO* images were drizzled assuming that there were no geometrical distortions in the images so that rows and columns were always assumed to be parallel and equally spaced. The 6.7-μm images was subsampled to one-third of the input pixel size, resulting in output pixels of 1 arcsec. The input pixel footprint was set to 0.65 and the pixel weights were taken from the reciprocals of the variances. The 15-μm images were subsampled to one-half of the input pixel size, resulting in output pixels of 3 arcsec. The footprint was again set to 0.65 and the same weighting scheme was used.

The drizzle code preserves flux by sharing the input levels amongst the output pixels. To return the output images to intensity units, the 15-μm images were multiplied by 4 and the 6.7-μm images by 9. The input weights were the reciprocals of the variances, and, to convert the output weights from the drizzle code back into a variance, a multiplying factor of 1/footprint^2 (2.367) had to be applied. These output variances are not totally independent, as each has contributions from neighbouring pixels.

The 15-μm (LW-3) image for field WF-4 appears to have incorrect astrometry in that, when the appropriate offset was applied, the sources did not line up exactly with the sources in field WF-2 or WF-3. An empirical offset was calculated using the CORREL_IMAGES routine from the IDL astrolib library (http://idlastro.gsfc.nasa.gov/homepage.html) to cross-correlate the images, and from visual checking. The resultant shift was 6.4 arcsec in the detector x-direction and -0.7 arcsec in the y-direction.

To ensure that the final mosaics were not affected by global variations in the background, the medians from the drizzled images of the individual points were compared and a multiplying factor (listed in Table 2) was applied to all the frames making up a pointing to bring them to the same level. The final drizzled images were then recomputed.

2.5 Flux calibration

To estimate the sky background, we constructed histograms of pixel counts for the central third of the unnormalized drizzled maps of each individual field. We fitted Gaussians to each of these histograms, and the resulting sky levels are listed in Table 2. The relative sky levels are in excellent agreement with the relative normalizations calculated above. A slightly more sophisticated procedure was adopted for the noise estimates. We selected a grid of positions in the central ~one-third of each drizzled mosaic, and placed a circular aperture of the Airy disc size on each position. We could then estimate the noise level on the scale of the Airy disc from the histogram of counts enclosed by these apertures.

Flux calibration assumes the standard conversion in the CAM handbook. In Table 2 we compare our background measurements with a zodiacal background model. This model linearly interpolates between entries in table 8 of the CAM Observer's Manual, but assumes a 275-K blackbody zodiacal spectrum (Hauser et al. 1984) rather than the alternative in the manual. The solar elongation angle at the time of our observations was approximately 71°.3. The cirrus contribution at both wavelengths is expected to be <2 per cent of the zodiacal background.

The sky calibration appears on the whole to be quite satisfactory. Checks on the calibrations using the sky, such as these, do not of course check the linearity of the response to sources, which may be very difficult to address with the *ISO* HDF data. It may nevertheless be possible to estimate this by examining the average temporal profiles of detected sources. Further discussion on the sensitivity to point sources is contained in Paper II.

3 RESULTS

3.1 Comparison of maps

Figs 2 and 3 (opposite p. 460) show the results of the drizzling algorithm. The correspondence between the drizzling and the shift-and-add mosaics (not shown) is excellent, suggesting that neither algorithm is introducing artefacts. Figs 4 and 5 show the coverage maps at the two wavelengths. Note the poorer coverage at the edges, which causes the poorer signal-to-noise ratio at the corresponding edges of the mosaics.

3.2 Source confusion

Several sources are clearly seen at 15 μm, and the source identification will be discussed in a later paper. However, we note here that a visual inspection clearly shows that we are approaching the confusion limit of one source per 40 beamsizes.

One surprising feature in the 6.7-μm maps is the apparent sky fluctuations at around 3 per cent of the background, which may be caused by source confusion, or by glitch transients which have been smeared out by the mosaicking pro-

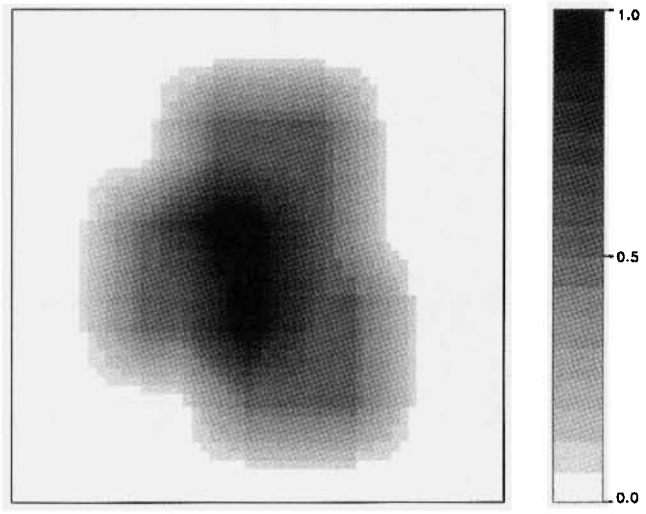

Figure 4. Coverage map at 6.7 μm. Note the poor coverage at the edges. The scale converts the grey levels to the relative coverage.

Opposite p. 460, MNRAS, **289**

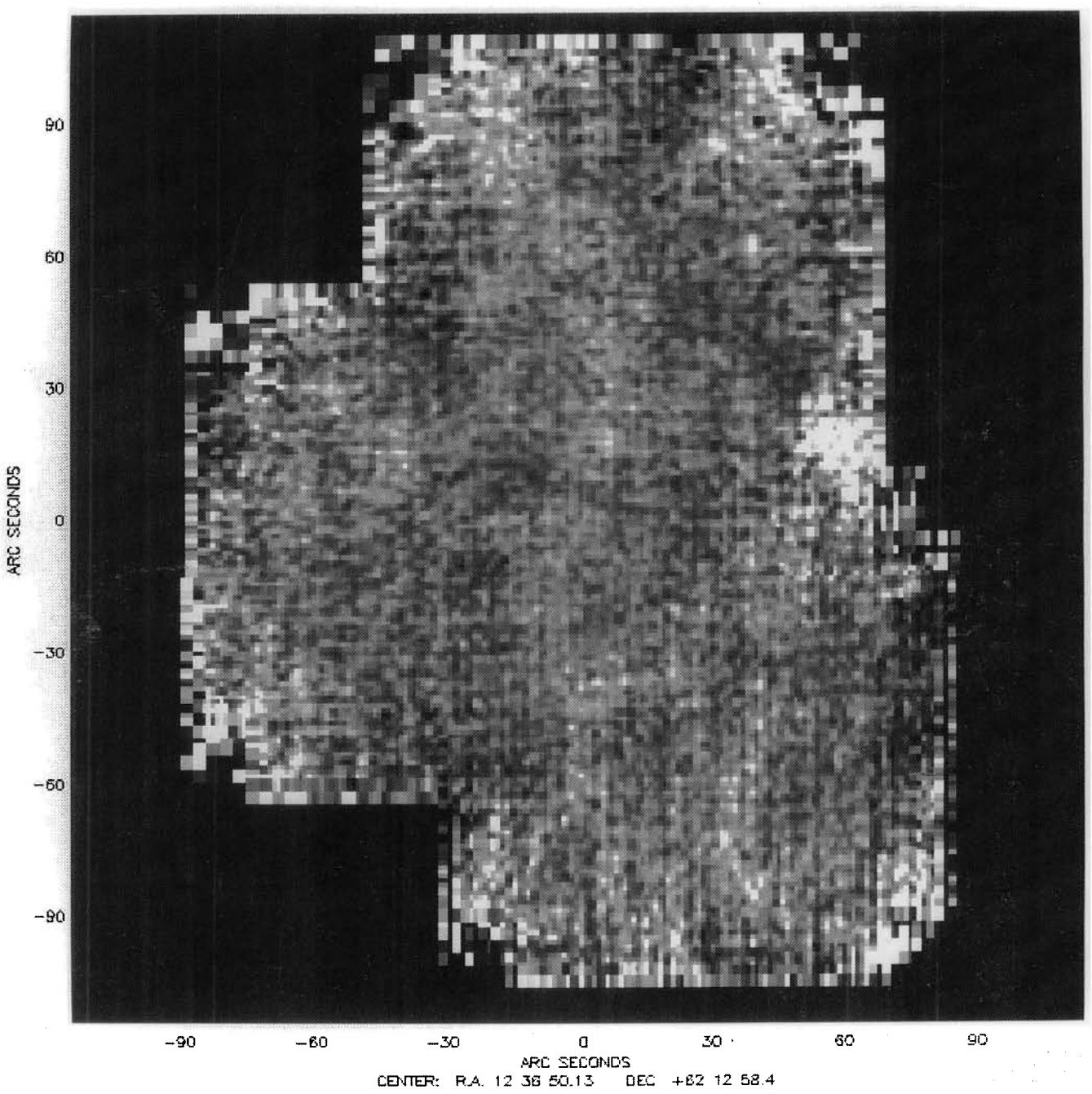

Figure 2. Drizzled mosaic at 7 μm. North is approximately 10° right of vertical, and east is to the left.

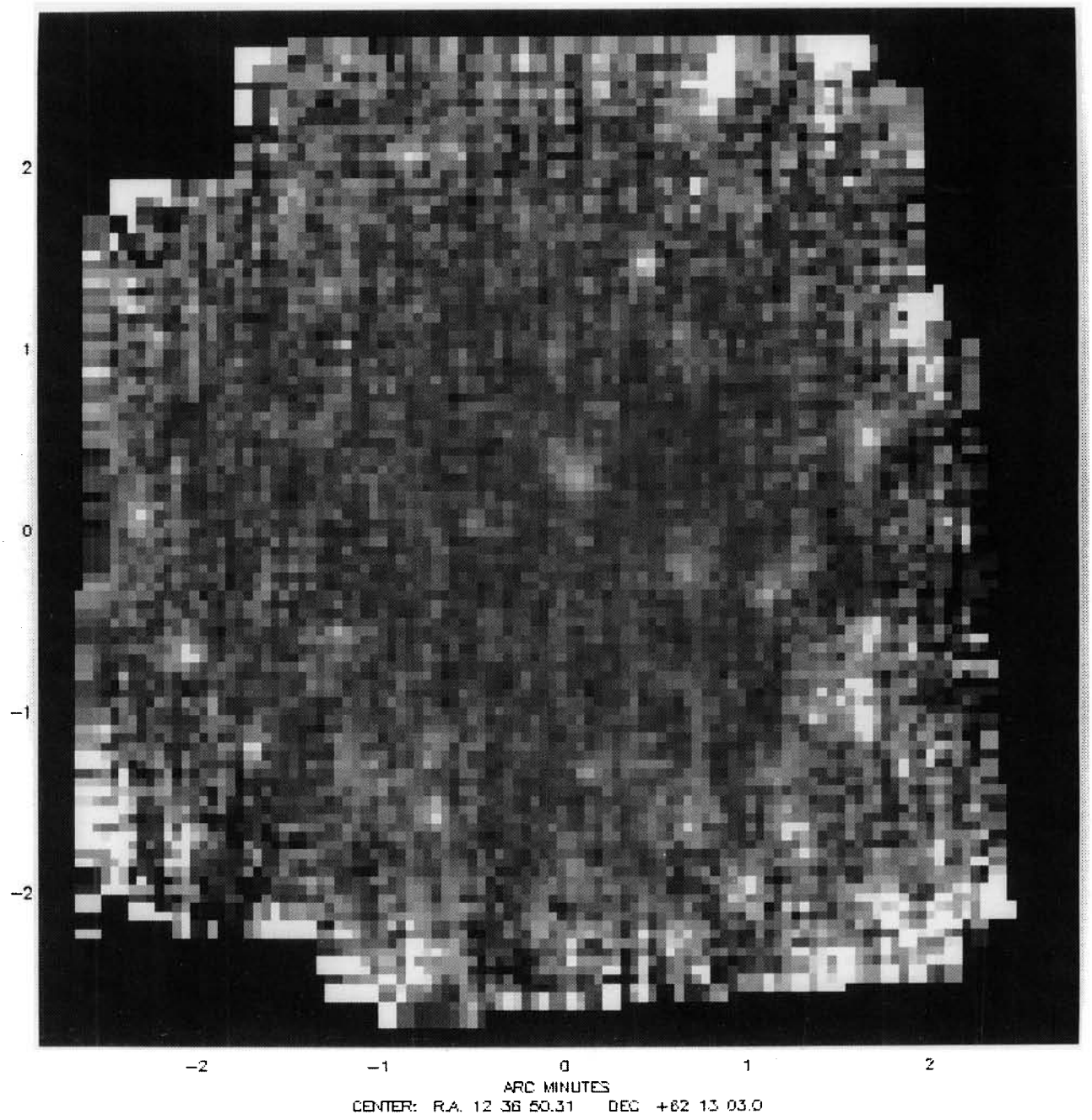

Figure 3. Drizzled mosaic at 15 μm.

cess. We tested this by taking ratios of each of the 6.7-μm shift-and-add mosaics. One apparent (albeit dubious) source was less prominent with increasing median filtering, so is a good candidate for such a smeared-out transient. Apart from this, the ratios of the 6.7-μm shift-and-add mosaics are flat to ~1 per cent accuracy, and do not have structures corresponding even roughly to the observed 6.7-μm maps. This suggests that the fluctuations are not an artefact of transients or flat-field errors, but are due to marginally detected sources.

A more convincing demonstration was made by shuffling the CAM pixels at random and making mosaics. The resulting frames should be equally susceptible to smeared-out transients, but genuine sources and background structure should be dispersed evenly over the mosaic. These randomnized frames show much less structure than the real frames (e.g. Fig. 6), again suggesting that this structure is not an instrumental artefact.

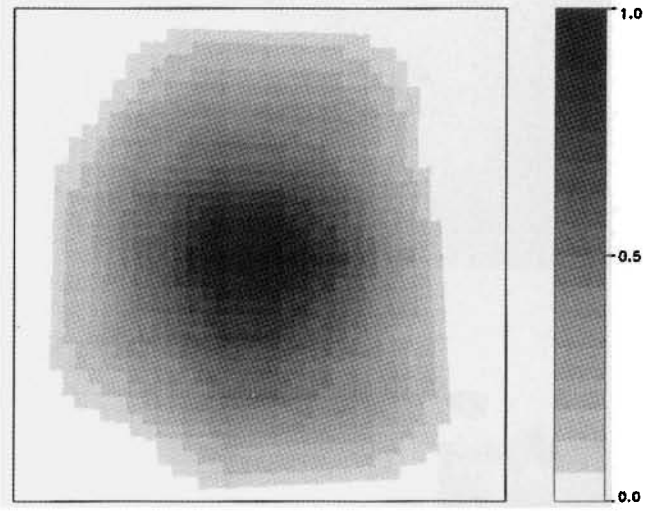

Figure 5. Coverage map at 15 μm. As with the 6.7 μm counterpart, the coverage is poor at the edges.

Note, however, that this does not test for the presence of correlated pixel-to-pixel flat-field variations. If such transient effects were present, they would be indistinguishable from genuine sky structure in the mosaicked images, and would be extremely difficult to remove in the data reduction process without also removing genuine structure. (It is nevertheles not clear how such correlated fluctuations would arise.) One approach to testing this is to rotate or reflect the arrangement of the CAM detector pixels, but repeat the same mosaicking as before. Any sky structure will be dispersed over the image (although not necessarily evenly), but the resulting images would be equally sensitive to structure from correlated pixel-to-pixel fluctuations. These images should therefore show less structure than the correctly mosaicked images. Fig. 6 shows an example of this test, and the frame does indeed show less structure than the correctly mosaicked frame. However, it is not clear how much of the remaining structure is due to unevenly dispersed, genuine sky structure, and how much is due to correlated pixel noise. These potential artefacts are still under investigation, but in the meantime it should be noted that some of the structures may potentially be due to instrumental artefacts.

Finally, a comparison of suitably smoothed drizzled and *HST* F814W images, discussed in the next section, shows remarkable correspondence.

3.3 Field distortion

To compare the apparent low-level sky fluctuations with the underlying HDF galaxy distribution, we convolved the drizzled *ISO* mosaics with an empirical point spread function (Paper II; Paper III). In Figs 7 and 8 we show a grey-scale reproduction of the F814W HDF and flanking fields.[2] Contours of our smoothed drizzled *ISO* mosaics are overlaid.

[2]The flanking field image (unfortunately without astrometry) is obtainable from
http://www.stsci.edu/ftp/science/hdf/project/flanking.html

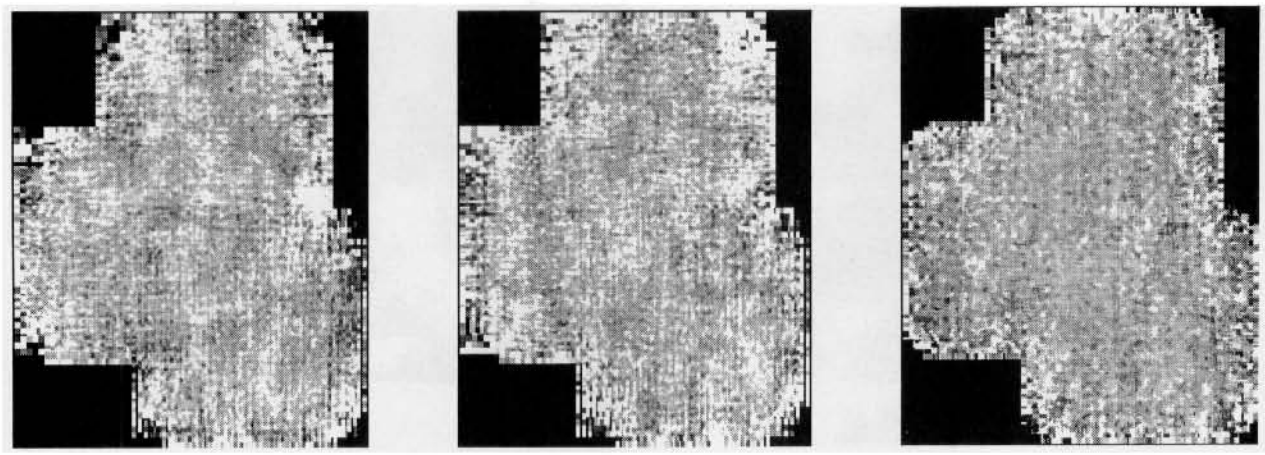

Figure 6. Comparison of the 6.7-μm drizzled image (left) with a similar (shift-and-add) mosaic made after randomizing the CAM detector pixel positions (right), and a drizzled mosaic obtained after rotating the CAM detector array through 90° (centre). As argued in the text, the drizzling and shift-and-add methods (not compared here) are found to be in excellent agreement. Note the lack of structure in the randomized frame, and the less prominent structure in the rotated-detector frame. As discussed in the text, the latter attempts to disperse any true structure on the sky over the image, while being equally sensitive to correlated pixel noise.

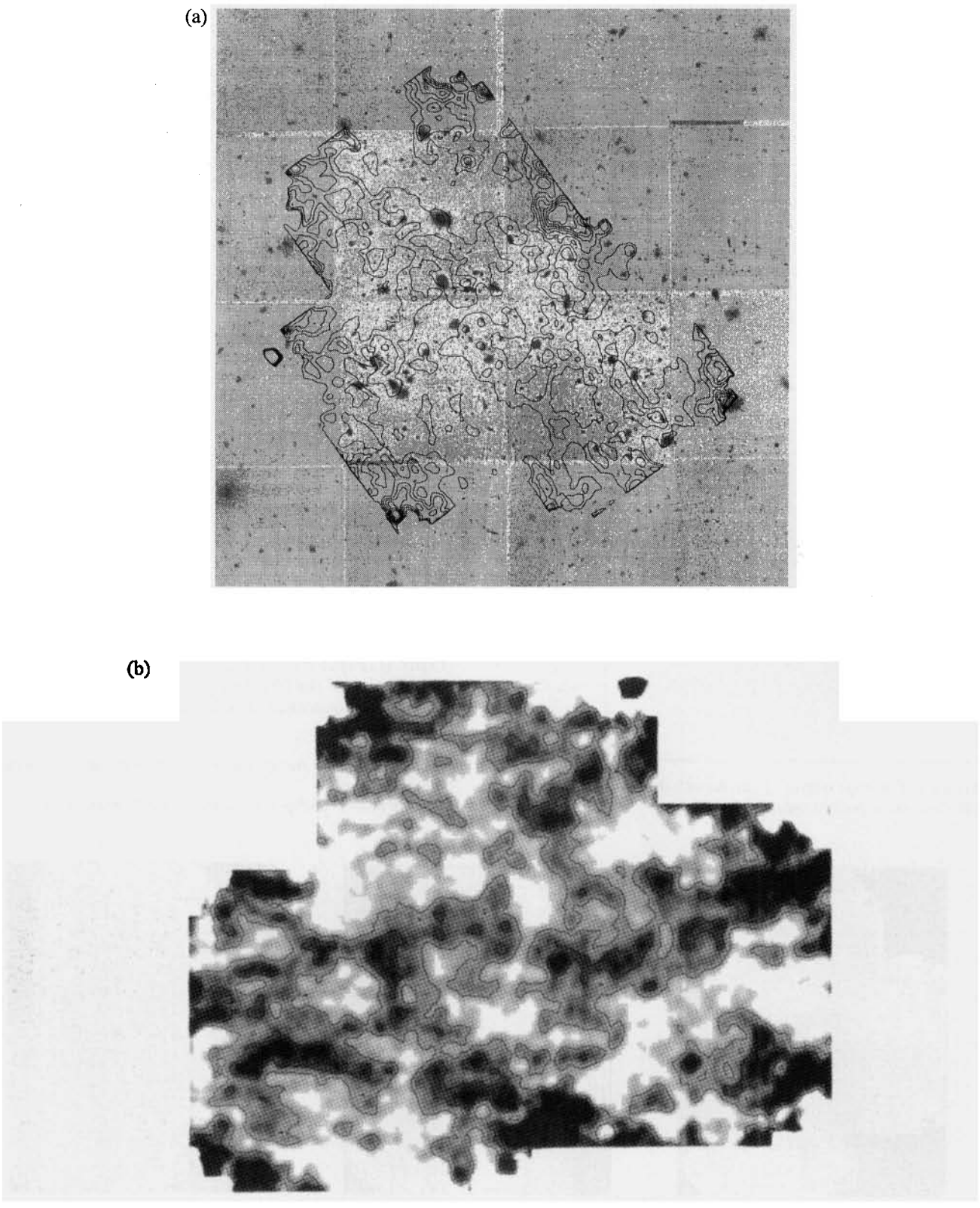

Figure 7. (a) The *HST* F814W image overlaid with contours of the smoothed drizzled 6.7-μm image discussed in the text. (b) The smoothed drizzled 6.7-μm image discussed in the text, with contours overlaid.

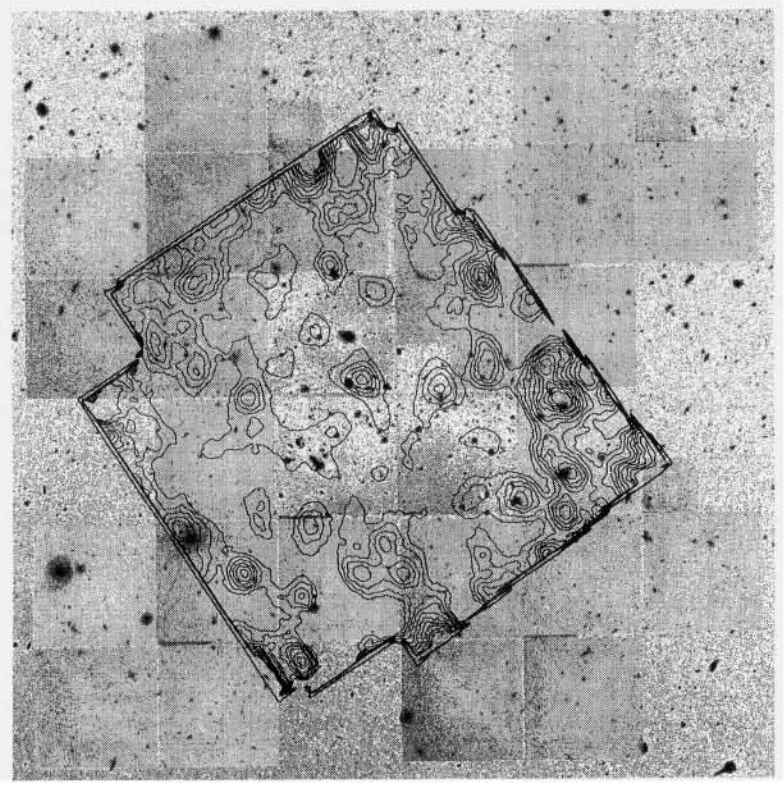

Figure 8. The *HST* F814W image overlaid with contours of the smoothed drizzled 15-μm image discussed in the text.

Two important points should be noted: first, the apparent low-level structures do indeed match the inhomogeneous galaxy distribution in the *HST* F814W frame, at least at 15 μm; secondly, this match is not perfect, suggesting an unknown astrometric error.

The astrometric errors do not appear to be random, but rather are systematic and varying continuously over the field. This is unlikely to be due to telescope pointing and lens positioning errors, since these would produce a non-varying systematic offset (recall that the individual rasters were registered with respect to each other). A likely explanation for the slight astrometric errors is therefore field distortion in CAM, i.e. the CAM detector array is not quite square. In-flight calibration of this distortion by the CAM consortium is currently underway; preliminary results indeed suggest that the total field distortion is about one pixel over the whole array, and that the distortion is continuous. Once this distortion is quantified, we expect to release appropriately revised mosaics. In the meantime, further papers in this series will conservatively treat the astrometry as subject to random errors of the order of the Airy disc size.

At 6.7 μm the structure, if present, is close to the noise; nevertheless, there are clearly several marginally detected sources at the positions of bright galaxies in the HDF F814W image: for example, several bright galaxies in field 2 (top left HDF frame) lie on or close to contour peaks. Note that the signal-to-noise ratio decreases sharply towards the edges, resulting in many features without apparent *I*-band counterparts. Finally, recall that correlated pixel-to-pixel flat-field variations (if present) would mimic real sky structure. Nevertheless, at least some of the structure appears to be marginally detected or unresolved sources.

4 DISCUSSION

Visual inspection of the maps at 6.7 and 15 μm clearly shows many sources, and these will be discussed further in the following papers. At these wavelengths the radiation is increasingly dominated by the reprocessing of starlight by dust, and it is to be expected that the detected galaxies have above average star formation rates. Our data demonstrate that *ISO* can detect galaxy populations comparable to those in faint optical surveys, and may also have implications for proposed confusion-limited surveys at around our wavelengths, such as that from the *WIRE* satellite. However, we defer a more extensive discussion of the confusion limit to Paper III.

These results are also promising for surveys at other wavelengths. Mobasher et al. (1996) combined their HDF photometric redshift data base with a starburst spectral energy distribution model and the HDF galaxy counts, to obtain predictions for cumulative number counts of HDF galaxies at wavelengths longward of 6.7 μm. Their expectation of ~tens of sources at *ISO* wavelengths at our approximate limiting flux densities per beam is clearly seen to be broadly correct. A detailed comparison with source count models is included in Paper III; however, we note here that Mobasher et al. also used the same models to predict ~one hundred sources in the HDF at both 60 μm and 0.8 mm to ~10–100 μJy levels. Our results are thus clearly encourag-

ing for SCUBA and the proposed large millimetre arrays, as well as for planned future infrared space missions such as *FIRST* and *SIRTF*.

Further information on the *ISO* HDF project can be found on the *ISO* HDF World Wide Web pages (http://artemis.ph.ic.ac.uk/hdf/).

ACKNOWLEDGMENTS

This paper is based on observations with *ISO*, an ESA project with instruments funded by ESA member states (especially the PI countries: France, Germany, the Netherlands and the United Kingdom) and with the participation of ISAS and NASA. This work was supported by PPARC (grant number GR/K98728) and by the EC TMR Network programme (FMRX-CT96-0068).

REFERENCES

Cesarsky C. et al., 1996, A&A, 315, 32
Fomalont E. B. et al., 1996, preprint
Fruchter A. S., Hook R. N., 1996, in Tanvir N. R., Aragon-Salamanca A., Wall J. V., eds, Proc. 37th Herstmonceux Conf. World Scientific Press, Singapore, in press (http://www.stsci/edu/~fruchter/dither/drizzle.html)
Goldschmidt P. et al., 1997, MNRAS, 289, 465 (Paper II, this issue)
Hauser M. G. et al., 1984, ApJ, 278, L15
Kessler M. et al., 1996, A&A, 315, L27
Mann R. G. et al., 1997, MNRAS, 289, 482 (Paper IV, this issue)
Mobasher B., Rowan-Robinson H., Georgakakis A., Eaton N., 1996, MNRAS, 282, L7
Oliver S. J. et al., 1997, MNRAS, 289, 471 (Paper III, this issue)
Pearson C., Rowan-Robinson M., 1996, MNRAS, 283, 174
Rowan-Robinson M. et al., 1997, MNRAS, 289, 490 (Paper V, this issue)
Williams R. W. et al., 1996, AJ, 112, 1335